

Modeling and characterization of the nucleation and growth of carbon nanostructures in physical synthesis

Journal Article**Author(s):**

Rossi, Kevin; Förster, Georg Daniel; Zeni, Claudio; Lam, Julien

Publication date:

2023-06

Permanent link:

<https://doi.org/10.3929/ethz-b-000615003>

Rights / license:

[Creative Commons Attribution-NonCommercial-NoDerivatives 4.0 International](#)

Originally published in:

Carbon Trends 11, <https://doi.org/10.1016/j.cartre.2023.100268>

Funding acknowledgement:

824143 - MAterials design at the eXascale. European Centre of Excellence in materials modelling, simulations, and design (EC)



Modeling and characterization of the nucleation and growth of carbon nanostructures in physical synthesis

Kevin Rossi^{a,e}, Georg Daniel Förster^b, Claudio Zeni^c, Julien Lam^{d,*}

^aLaboratory of Nanochemistry for Energy, ISIC, Ecole Polytechnique Fédérale de Lausanne, Sion 1950, Switzerland

^bInterfaces, Confinement, Matériaux et Nanostructures, ICMN, Université d'Orléans, CNRS, Orléans, France

^cInternational School for Advanced Studies, Via Bonomea, 265, Trieste, 34136, Italy

^dCEMES, CNRS and Université de Toulouse, 29 rue Jeanne Marvig, Toulouse Cedex 31055, France

^eInstitute for Chemical and Bio-engineering, Department of Chemistry and Applied Biosciences, ETH Zurich, Vladimir-Prelog-Weg 1, 8093 Zurich, Switzerland

ARTICLE INFO

Keywords:

Carbon formation
Molecular dynamics
Carbon characterization
Carbon gas nucleation and growth

ABSTRACT

Carbon nanostructures formed through physical synthesis come in a variety of sizes and shapes. With the end goal of rationalizing synthetic pathways of carbon nanostructures as a function of tunable parameters in the synthesis, we investigate how the initial density and quench rate influence the morphology of carbon nanostructures obtained from the cooling of a gas of atomic carbon by molecular dynamics simulations. For the structural analysis, we combine classical order parameters with a data-driven approach based on local density descriptors and kernel similarity measurements. Aided by this complementary set of tools, we describe in detail the formation of carbon nanostructures from the gas phase. Their formation proceeds through the nucleation of small liquid carbon nanoclusters followed by growth into unique objects. We find that ordered structures can only be obtained at certain quenching rates and that among those, fullerene-like particles are favored at intermediate densities while nanotubes-like structures require higher initial densities. © XXXX CEA. Elsevier

1. Introduction

At the nanometric scale, carbon allotropes can be found in several different forms, including nanodiamonds, amorphous structures, nanotubes, nanosheets, and fullerenes. This diverse set of structures shows potential for numerous applications. The unique properties of carbon nanotubes – e.g. their extraordinary electric conductivity and mechanical response – is currently explored and exploited in research domains like tissue engineering [1], microelectronics [2,3], biomedical science [4,5], and material reinforcement [6]. Similarly, fullerene-like nanoparticles, i.e. spherical shells of carbon atoms, attracted an interest in catalysis [7] and in biological applications where they are used as e.g., anti-HIV, radical scavenger, radio-tracer, and antibacterial compounds [8,9].

Among different synthetic procedures, physical routes constitute a prominent family of methods to manufacture carbon-based nanomaterials, since they do not require the use of other chemical precursors. Generally, physical synthesis consists of an ablation step (e.g., via sputtering, laser, or combustion) to generate a hot, highly out-of-equilibrium gas, followed by the subsequent cooling of the ablated species, which leads to gas condensation and the formation of nanostructures. Laser ablation has been used to generate dense graphitic and diamond-like parti-

cles [10,11] in liquid as well as single-walled carbon nanotubes [12,13] and fullerenes [14] in gas. In addition, thin films of amorphous carbon were obtained using magnetron sputtering [15,16].

From an experimental standpoint, spectroscopy techniques have been instrumental in addressing the complexity of nucleation in out-of-equilibrium environments. In particular, Raman spectroscopy, Fourier transform infrared spectroscopy, laser-induced fluorescence, and plasma spectroscopy enable to probe the temperature of the system at the early stages of the gas condensation, when the latter is composed of clusters of few atoms and isolated carbon atoms [17]. Plasma spectroscopy can be used to measure the relative chemical composition, the temperature and electron density in the context of laser ablation [10,18,19]. Nevertheless, experiments still struggle to devise a fully detailed atomistic picture of nucleation during the nanostructure formation thus preventing from a rational control of the synthesis products.

In this context, simulations represent an ideal and complementary tool to study and rationalize the formation mechanisms in out-of-equilibrium conditions. Previous works using atomistic modelling have proven instrumental in the understanding of ablation mechanisms, using two-temperature models [20–24]. In addition, numerous numerical investigations enabled to derive an atomistic understanding of the gas condensation step in single element materials with different chemistries,

* Corresponding author.

E-mail addresses: k1992@hotmail.it (K. Rossi), julien.lam@cnrs.fr (J. Lam).

namely, silicon [25], germanium [26,27], and transition metals [28]. Similarly, the atomistic mechanisms occurring during the synthesis of binary systems with diverse chemical arrangements (e.g., alloyed, Janus and core-shell nanoalloys) were explored in the case of physical methods [29–32]. An emerging topic in numerical modeling of nanomaterials further concerns the simulation and study of phase changes from liquid to solid at the nanoscale [33,34].

In this work, we employ molecular dynamics simulations (MD) to reveal the mechanisms associated with the formation of carbonaceous nanoparticles in gas condensation. To characterize the condensation pathway and map the influence of the quenching rate and the gas density, we first monitor classical order parameters such as coordination numbers, as well as the length of the rings in each structure using Franzblau analysis. Then, we measure the similarity between archetypical reference structures and those obtained by gas condensation using a kernelized metric based on a local-density representation.

The combination of traditional topology-based order parameters and the local-density kernelized similarity metric allows us to quantitatively establish relationships between synthesis parameters and structure. We find that large annealing rates lead to amorphous carbon structures, while slow temperature annealing results in more ordered nanostructures. The gas density is also crucial in determining the morphology of the carbon nanostructure. In particular, the emergence of fullerene-like carbon particles can only be obtained at lower gas density while nanotube-like nanostructures are favored at higher gas density. Lower gas densities further favour the abundance of 3-coordinated carbon atoms and of atoms in 6-membered rings.

Our numerical simulations also provide a dynamical picture of the formation process. From a mechanistic perspective, we show that the gas phase synthesis of carbon nanostructures proceeds through three stages: 1) the nucleation of small carbon clusters, 2) the rapid growth of the carbon nanostructure, 3) a steady-state phase where local and minor rearrangements take place.

In the next section of the report, we detail the computational methods employed to perform and analyze the carbon nucleation and growth simulations. Then, we present the result of our simulations paired with an in-depth analysis of the influence of the quenching rate and gas density on the final structure, as well as on the nucleation and growth mechanism. The conclusion of the manuscript presents a brief overview of our main result as well as an outlook on the transferability of our approach to study other systems.

2. Computational methods

The accurate modeling and characterization of carbon nanostructures nucleation and growth from the gas phase demands for the combination of a number of techniques. This section details the employed numerical methods. We first describe and motivate our molecular dynamics set-ups. Then, we justify the choices made for characterizing the carbon nanostructures in terms of classical and modern order parameters.

2.1. Molecular dynamics

To simulate the nucleation and growth of carbon nanostructures from a gas, molecular dynamics simulations were carried out using the LAMMPS software [35]. The Tersoff potential [36,37] is adopted to model carbon interactions because of its efficiency [38] and fair accuracy [39]. Although there are many more recent carbon potentials [40–42], they usually lack the execution speed of the original Tersoff potential and/or are less widely used. The chosen Tersoff potential is very well known at least (also with its limitations) and has been successfully used to explain and predict the behavior of carbon systems in various environments, including high-pressure and high-temperature conditions [43]. In each carbon gas condensation simulations, the initial state of the system consists of 1000 carbon atoms randomly positioned in a cubic box.

The volume of the simulation box is fixed for the whole duration of the simulation. The system is then evolved according to Newton's equation of motion by means of a velocity-Verlet integration scheme, with a time-step of 1 fs. Motivation for the timestep value can be found in the SI. The temperature of the ensemble is enforced by a Nose-Hoover thermostat using a damping factor of 100 fs. The initial temperature is set to 10,000 K. The final temperature is 3,000 K.

For a systematic assessment of the influence of the quenching rate and the gas density on the final nanostructures, we consider 5 different gas densities, corresponding to 5 simulation box edge of – i) 0.312 g/cm³ (40 Å box edge), ii) 0.092 g/cm³ (60 Å box edge), iii) 0.039 g/cm³ (80 Å box edge), iv) 0.020 g/cm³ (100 Å box edge), v) 0.012 g/cm³ (120 Å box edge) – and 6 different quenching rates – i) 700 K/ns, ii) 350 K/ns, iii) 140 K/ns, iv) 70 K/ns, v) 35 K/ns, vi) 14 K/ns – for a grand total of 30 different simulation conditions. For each of the situations, indeed, 5 independent simulation runs have been carried out. These were initialized from different random initial positions of the atoms and different initial velocities. All the other simulation parameters are identical among each group of 5 runs.

The chosen gas densities and cooling rates span considerable magnitudes and include synthesis conditions relevant to experiments thus allowing for an informative and comprehensive picture of the relationship between synthesis parameters and carbon nanostructure morphologies. This is particularly relevant for laser synthesis methods like laser ablation in liquid or pulsed laser deposition, where the cooling from gas occurs via extremely rapid quenching [10]. In Ref. [10], no temperature higher than 6000 K was measured because the experiments rely on the plasma emission spectroscopy from C₂ molecules that only appear below approximately 6000 K as evidenced by our current calculations. Yet, in Ref. [19], it is shown by using plasma emission spectroscopy from atomic species, that the temperature can go up to 1.5×10^4 K. In addition, regarding the quenching rates, we chose to study different values that are located below and above the experimental measurements.

2.2. Numerical analysis

2.2.1. Topological descriptors

We characterize carbon nanostructures by means of topological order parameters commonly used in the literature, namely, the population of n -coordinated ($n = 2, 3$) carbon atoms and of 6-membered carbon rings. To evaluate the coordination of a carbon atom, we count the number of neighbors within a cut-off of 1.7 Å. We choose this distance because it includes the entire first neighbor shell of graphite and diamond and excludes second neighbors in case of the two crystals. Atoms which are neighbors share a bond. The number of bonds in a ring defines its length, which we analyze using Franzblau statistics [44] as implemented in the polypy [45] code.

To evaluate global order parameters, i.e., inertia tensor descriptors and similarity kernel measures, we look at the largest connected clusters sampled during the dynamics.

Atoms are grouped together into clusters based on a simple distance cut-off criterion of 2 Å possibly across periodic boundaries.

2.2.2. Inertia tensor descriptors

We assess the degree of anisotropy and the density of the carbon nanostructures by monitoring global order parameters derived from the gyration tensor. Let λ_i label the diagonal elements of the gyration tensor, ordered so that $\lambda_x^2 < \lambda_y^2 < \lambda_z^2$ the squared radius of gyration is found equal to:

$$R_g^2 = \lambda_x^2 + \lambda_y^2 + \lambda_z^2 \quad (1)$$

The asphericity parameter reads [46]:

$$A2 = \frac{(\lambda_x - \lambda_y)^2 + (\lambda_y - \lambda_z)^2 + (\lambda_z - \lambda_x)^2}{2(\lambda_x + \lambda_y + \lambda_z)^2} \quad (2)$$

For reference, when considering a fixed number of atoms, larger radii of gyration correspond to larger volumes and smaller densities. The asphericity parameter ranges from 0 (spherical) to 1 (cylindrical) [46].

2.2.3. Similarity with respect to reference archetypes

Along these two traditional approaches of structural characterization, we also consider a data-driven approach based on kernel similarity measurements and local density descriptors.

Local density descriptors For each atom, we assign a set of 69 features within the Atomic Cluster Expansion (ACE) framework [47], where the descriptors are computed as described in Dussan et al. [48] using the Julia ACE package [49]. This representation is smooth by construction, invariant to rotation, translation, and permutation of identical atoms, and allows for a characterization of the local atomic environment that does not depend on hand-crafted features. The ACE descriptors are furthermore able to encode many-body correlations (here limited up to 4 because of the corresponding computational complexity to go beyond this number), and offer a descriptive representation of the local geometry around atoms. A similar approach has been successfully employed in statistical learning methods to map structure-property relationships [50–53].

Reference Archetypes Similarity measures between sets of features deriving from local density representations are a well-established tool in the prediction and/or rationalization of structure-property relationships [50–52]. Here, a kernel approach is employed to measure the similarity between the atomic environments sampled in the nanostructures and known structures found in fullerenes, nanotubes, and bulk amorphous carbon, which constitute a database. The reference structures are depicted in Fig. S2 of the supplemental material. In particular, we measure the similarity with respect to each family of archetypes by considering:

- 3 bulk amorphous carbon configurations with different densities, corresponding to 1000 carbon atoms in periodic boxes of edge length between ~ 20 Å and ~ 30 Å.
- 8 different nanotubes with diameters between ~ 10 Å and ~ 20 Å.
- 8 different fullerenes with diameters between ~ 10 Å and ~ 30 Å.

The archetypes are chosen to encompass densities (for periodic systems) and diameters (for fullerenes and nanotubes) which were expected to be comparable to the ones obtained in our simulations.

From an operative perspective, we first compute the ACE descriptors and perform an averaging over all the atoms within the largest connected cluster in each structure I : $\mathbf{Q}_I = \sum_{i \in I} \mathbf{q}_i / ||I||$, where $||I||$ indicates the number of atoms contained in the largest connected cluster of I . We then normalize \mathbf{Q}_I , yielding the unit vector $\hat{\mathbf{Q}}_I$ pertaining to structure I . We include only non-isolated atoms into the analysis since we aim to classify the carbon structures forming during the nucleation and growth process, and the inclusion of local atomic environments from isolated atoms would add noise to the characterization process. We then measure the similarity $k(\hat{\mathbf{Q}}_I, \hat{\mathbf{Q}}_J)$ between pairs of structures (I, J) by adopting the following Radial Basis Function (RBF) kernel:

$$k(\hat{\mathbf{Q}}_I, \hat{\mathbf{Q}}_J) = \left\langle \exp \left(-\frac{(\hat{\mathbf{Q}}_I - \hat{\mathbf{Q}}_J)^2}{2\sigma^2} \right) \right\rangle \quad (3)$$

where the average is taken over the D features of the descriptors, and σ is set to 0.001. This value of σ is the one that maximizes the standard deviation of similarity scores among all trajectories and references, allowing for better discrimination. Additional details on the choice of σ can be found in the Supplementary Information.

The above procedure yields a similarity score between 0 and 1 for each pair of structures, with 1 being the most similar. This score does not depend on the size of the systems, and is invariant to the physical symmetries relevant to the comparison of different structures. We note that other choices in terms of descriptor space, normalization approach, averaging methods and similarity kernel were possible while leading to

slightly different quantitative scores. Yet, we verified that the reported findings preserve the same qualitative information when, e.g., different cut-off distances, number of features in the representation, or different (but still reasonable) archetype representatives are chosen.

3. Results and discussion

3.1. Influence of the quenching rate and the gas density on final morphologies

Our first objective is to investigate the interplay between gas density and quenching rate in determining the final structure of nanoscale carbon.

Qualitative differences between the nanostructures can be inferred from a simple visual inspection. A visual representation of the carbon nanostructures sampled at the end of paradigmatic trajectories – over the full set of gas densities and quenching rates considered in this work – is shown in Fig. 1. The structures sampled from rapid annealing are defective and have concave surfaces. They also exhibit a large number of carbon atoms inside otherwise hollow nanostructures. Structures obtained at the end of slow annealing trajectories appear, on average, more regular, and their surface comprises fewer defects. Furthermore, the majority of the carbon atoms lie at the surface of the final nanostructure in case of low annealing rates. We note artifacts at small box edge lengths (40 Å, and 60 Å to a lesser extent), where some finite-size effects appear: some nanostructures extend over the periodic boundary conditions imposed in the simulation (see also SI Figure S3 for further detail). This is however inevitable if we are to simulate the formation of nanotubes in finite simulation boxes of any size. Our discussion will thus focus in greater detail on simulations with box sizes larger than 60 Å.

For a more quantitative structural characterization, we collect structures from the last 2% of the annealing trajectory and average structural observables according to the classical and kernelized metrics discussed in the method section. The number of snapshots used for averaging is 10, 20, 50, 100, 200, and 500 in the case of quench rates of 700 K/ns, 350 K/ns, 140 K/ns, 70 K/ns, 35 K/ns, and 14 K/ns, respectively. Fig. 2 A illustrates characterization through coordination-based descriptors. By decreasing the cooling rate and increasing the gas density, the number of 3-coordinated atoms and the number of atoms in 6-membered rings can be increased. The population of 2-coordinated atoms follows the opposite trend with respect to cooling rates and gas densities, i.e., higher cooling rates and lower gas densities result in an increase of 2-coordinated atoms. We then note that 6-rings and 3-coordinated atoms are indicative of higher-stability structures. We conclude that, when the quenching is slow enough, the system has more time to explore the energy landscape, and find lower potential energy minima. In case of fast quenching, the system gets trapped in energetically less favorable configurations, including under-coordinated carbon atoms. These more open structures (i.e., including many 2-coordinated atoms) also occur at lower density, where quenching is less effective in exploring energy minima.

As a next step in our structural characterization, we look at inertia tensor-based descriptors, which is complementary to the one of n -coordinated atoms and rings statistics. Indeed, the radius of gyration and the asphericity of the structures are global (i.e., related to the entire structure) order parameters. To analyze these aspects quantitatively, we report in Fig. 2 B, the average radius of gyration and asphericity of the obtained nanostructures, as a function of the gas density and quenching rate. No monotonic trends are identified for these two descriptors. At the highest density, both gyration radii and asphericity are high, in agreement with visual inspection (see also Fig. 1). Indeed tube-like structures are found for the smaller boxes. At the other extreme of low densities, structures are less regular, and therefore both indicators are increased with respect to the minimal values found for a box edge length of 60 Å. This is the smallest size under consideration where most

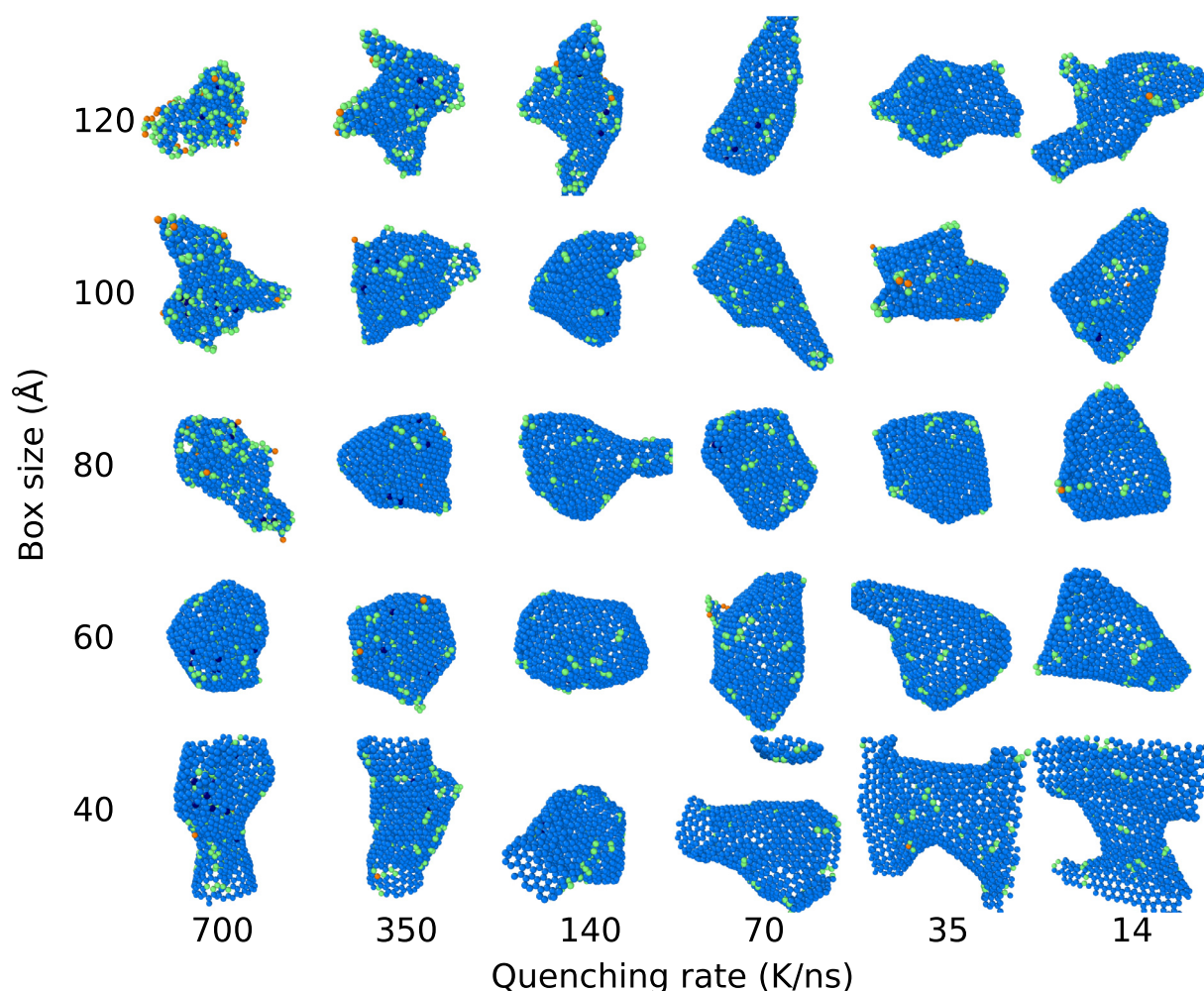


Fig. 1. Snapshots of examples of final configurations sampled from the end of annealing trajectories, arranged according to the initial gas densities and quenching rates. Atoms are color-coded according to their coordination (dark blue=4-fold coordinated, light blue=3-fold coordinated, green=2-fold coordinated, and orange=1-fold coordinated). (For interpretation of the references to colour in this figure legend, the reader is referred to the web version of this article.)

regular fullerenes are formed. The gyration radii tend to decrease with the quenching rate. This can be attributed to the fact that hollow particles are formed when given enough time during the annealing. More amorphous and dense particles occur at higher quenching rates, when the systems are forced into more out-of-equilibrium configurations.

At this stage, using only classical order parameters, it remains difficult to fully characterize the observed structures. In particular, for the ordered structures obtained with slow annealing, we cannot discriminate well between nanotubes and fullerene-like structures. To alleviate this difficulty, we will now switch to our data-driven approach for structural characterization. Fig. 2 C shows the average local environment similarity regarding the archetypical structures (amorphous bulk, fullerenes, and nanotubes) mentioned in the method section. First, we confirm that rapid annealing and low densities lead to amorphous structures, an observation which was already made by the classical analysis.

In agreement with visual inspection, structures that do not display carbon atoms enclosed by an outer shell are the ones whose similarity to fullerenes and nanotubes is the largest. An assessment of finite-size effects (Figure S3) shows that the trends also hold when considering a smaller (500 atoms) or larger (2000 atoms) number of atoms and a fixed density. The similarity to fullerene increases when decreasing the gas density and for intermediate quenching rates located between 35 K/ns and 140 K/ns. Meanwhile, the similarity to nanotubes increases at the

lowest quenching rates. Yet, we observe a non-monotonic behavior since intermediate gas densities are required to form of nanotube-like structures. In this case, the results of the data-driven approach correlates very well with coordination-based analysis. High numbers of 3-coordinated atoms and 6-membered rings occur in conditions where similarities with fullerenes and nanotubes are highest.

Coordination statistics can provide some amount of structural information, while similarity measures based on features deriving from a local density representation can better distinguish between carbon allotropes consisting only of 3-coordinated atoms and mostly six-membered rings, such as fullerenes and nanotubes. While this information can be partially inferred from global observables such as the radius of gyration and asphericity, atom density representation provide a straightforward avenue to interpret the similarity measure according to local contributions. The similarity measures are also able to distinguish correctly between highly defective amorphous elongated structures obtained at low density and high quench rates, and more nanotube-like objects, which we sample at lower quench rates. This resolution can be obtained notwithstanding the similarity of these configurations according to visual inspection (see also Fig. 1).

From our structural analysis combining classical order parameters along with data-driven approaches, we conclude that the gas density and the quenching rate are two control parameters of the structure of carbon-based nanomaterials synthesized via physical routes. Extremely

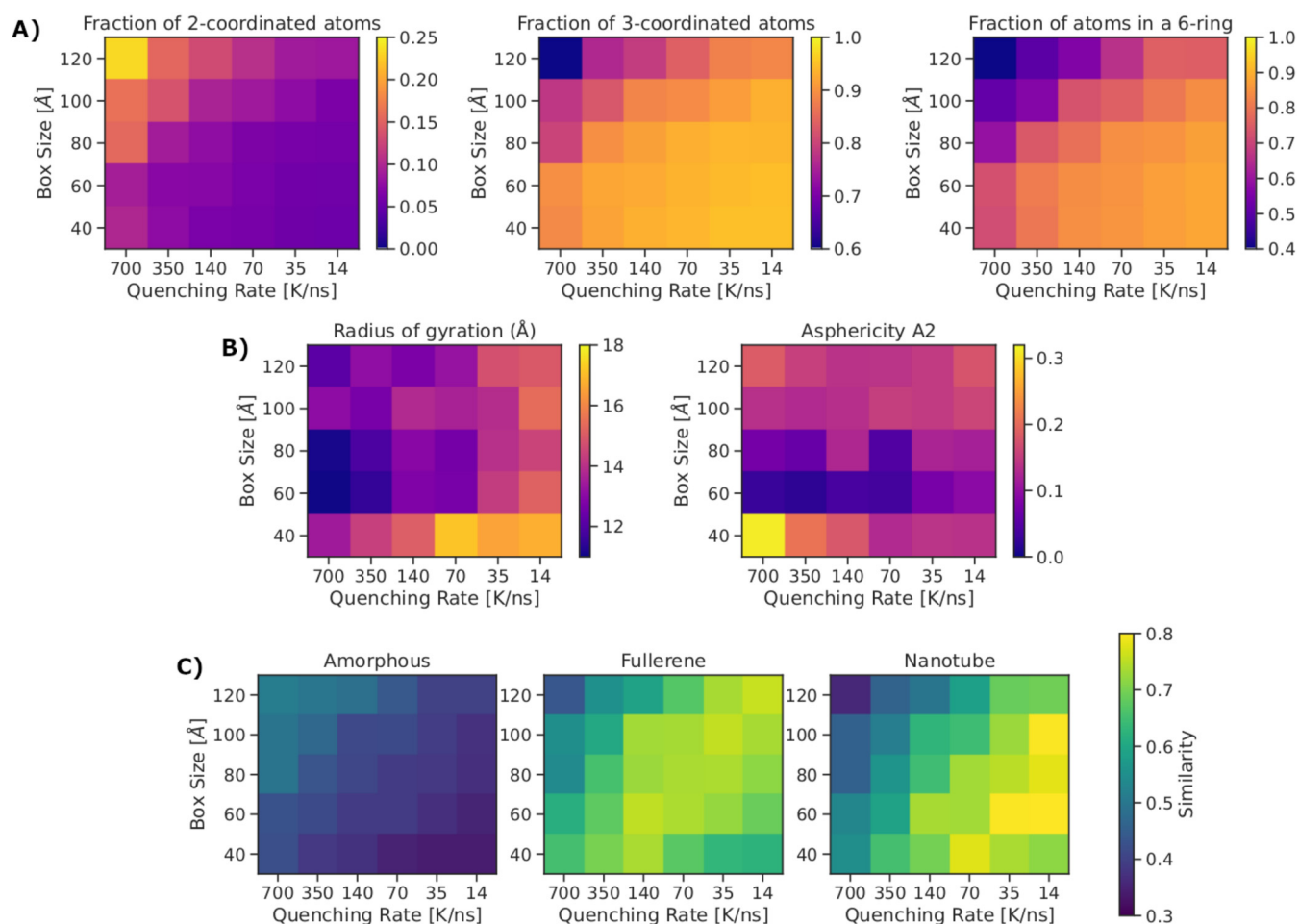


Fig. 2. A) Density versus quenching rate phase diagrams color-coded according to the fraction of 2-coordinated carbon atoms, 3-coordinated carbon atoms, and 6-membered rings. For the former two quantities we normalize by the number of atoms considered in the simulation (i.e., 1000), for the latter we consider the ideal case where each C atom participates in three 6-membered rings, and, in turn, normalize the total number of 6-membered rings by 500. B) Radius of gyration and asphericity of the largest connected carbon nanostructure versus quenching rate phase diagrams. C) Similarity regarding target structures - amorphous, fullerene, and nanotube, left to right - versus quenching rate phase diagrams. All data refer to data averaging over the final 2% of the trajectory for five independent runs.

fast quenching rates lead to amorphous nanostructures. If the annealing is slow enough to generate ordered structures, there exists a competition between fullerene- and nanotube-like nanostructures. In particular, fullerene-like nanostructures can only be obtained with intermediate quenching rates regardless of the density. The position of the observed transition highly depends on the gas density, the total number of available carbon atoms, and can hardly be compared with available experimental conditions. However, we expect the existence of a transition between fullerene-like and nanotube-like nanostructures, with the latter being preponderant at the lowest cooling rates.

3.2. Dynamical picture of the condensation

After having established the effect of gas density and quenching rate on the final carbon nanostructure, it is natural to proceed in characterizing the mechanism by which condensation occurs.

We begin by analyzing the number of carbon atoms in the largest connected cluster. As reported in Fig. 3, all the tested synthesis conditions lead to the formation of a single nanostructure comprising between 800 and 1000 atoms. For temperatures above 4500 to 6000 K, the largest connected cluster contains at most 10 atoms (beside for the cases where artifacts due to periodic boundaries can be non-negligible, i.e., for simulation box edges of 40 Å). The critical temperature at which a unique nanostructure appears depends on the gas density, with larger

density leading to larger critical temperature. The temperature at which a dominant nanostructure is formed is also determined by the quenching rate with higher transition temperatures found at higher quench rates. The temperature range over which the transition occurs is larger in case of the higher quench rates. Higher quenching rates correlate with larger critical temperatures. A less clear-cut trend is observed in the simulations with box sizes of 40 Å and 60 Å, a behavior ascribed to the previously mentioned finite-size artifacts.

For a more quantitative analysis, we set a somewhat arbitrary threshold of 200 atoms for the critical nucleus, after which the growth mechanisms starts. We find that this critical nucleus emerges at different temperatures, depending on the gas density. For box edges of 40 Å, 80 Å and 100 Å the latter appears respectively at $7100 \text{ K} \pm 60 \text{ K}$, $6380 \pm 100 \text{ K}$, or $5680 \text{ K} \pm 120 \text{ K}$. Therefore, increasing the gas density leads to a faster formation of the droplets. We note that the precise value of the size of the critical nucleus should only affect quantitatively the results but should lead to the similar qualitative picture.

In all of our simulations, formation pathways and kinetics do play an important role. Indeed, condensation products of varying degrees of metastability are obtained, with the more stable structures found at lower quench rates. We complement our analysis with a characterization of the evolution of the carbon nanostructures during the condensation process. This allows to understand the observations concerning the condensation products. For this discussion, we look at a fixed intermediate

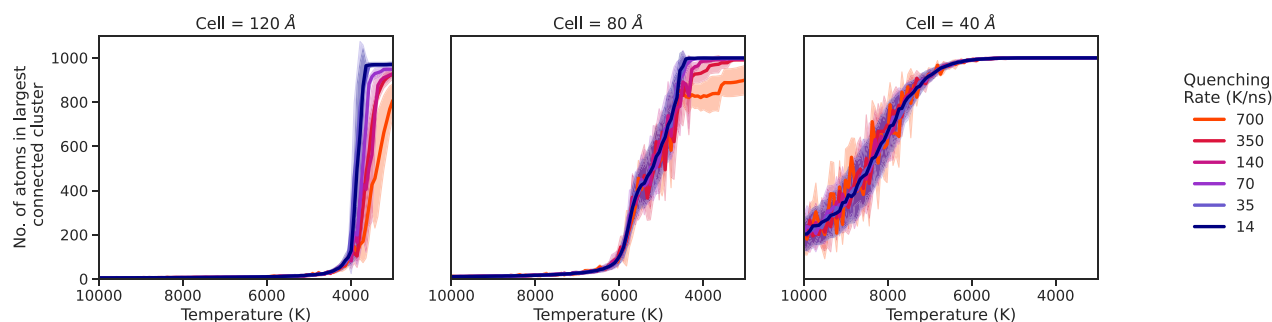


Fig. 3. Temperature-dependent evolution of the number of carbon atoms in the largest connected cluster found in the simulations.

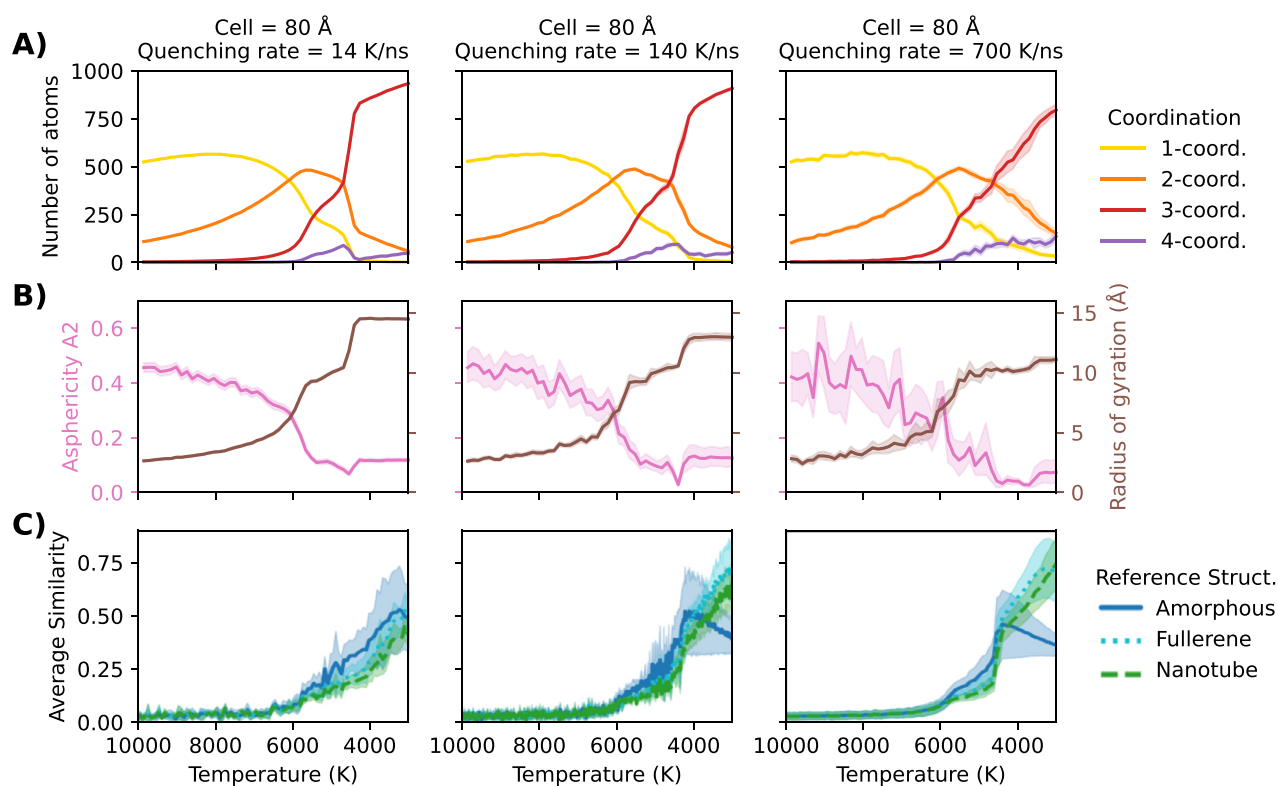


Fig. 4. Time- and temperature- dependent evolution for a fixed cell edge (80 Å) of the carbon coordination statistics (panel A), asphericity and radius of gyration of the largest connected carbon nanostructure (panel B) and the similarity between the carbon configurations sampled during annealing and the reference archetypes (panel C). The amount of 4-coordinated atoms has been exaggerated by a factor of 10 for better visibility. The three columns correspond to different quench rates indicated on top. Fig. S5 (supplemental material) compares the effect of the quenching rates directly in terms of 1-, 2-, 3-, and 4- coordinated atoms.

density (Cell size of 80 Å) so that potential finite size effects do not interfere with the analysis. Fig. 4 reports the evolution of several of the previously introduced structural indicators: (A) coordination numbers, (B) asphericity and gyration radii, and (C) the kernel similarity metric comparing to reference archetypes.

The initial conditions are the same in the three cases analysed in Fig. 4: an atomic gas of a density of 0.039 g/cm³ at 10000 K. Down to 6000 K, the evolution of the systems subject to the three different quench rates is very similar: atomic gas and short-lived mono-coordinated atoms (dimers) dominate the picture, with the dimer population reaching a smooth maximum at around 8000 K (yellow curve). Short chains (two-coordinated atoms) become more important at temperatures around 6000 K and peak at slightly lower temperatures. Asphericity and gyration radii are calculated here on the basis of the largest connected fragment, which consists of very few atoms in these early stages. In turn,

these indicators fluctuate significantly, and do not carry much information at the beginning of the simulations. By the same token, the similarity regarding the solid reference archetypes is close to zero, which is a clear indication that kernel similarity measurement does not lead to false positives when comparing to structures that are not in the reference database.

In the next step, most of the atoms condense into a single droplet, which is reflected by the fact that both the largest fragment (gyration radius) and the number of three-coordinated atoms (at the expense of mono- and two-coordinated atoms) increase significantly. Asphericity decreases and fluctuates less, which is also compatible with a (filled) droplet geometry. Remarkably, the similarity to bulk amorphous carbon already increases in the higher temperature ranges (6000–4000 K), meaning that the system transitions through a liquid-like phase that locally resembles amorphous carbon. This transition is sharper and oc-

curs at slightly higher temperatures in case of the lower quenching rates.

The subsequent evolution depends very much on the quench rate. In the case of the highest quench rate (left column in Fig. 4), this transition is very smooth and the process of atom addition from the gas phase continues until the end of the simulations. Movements of atoms in the largest cluster become more and more sluggish, until it turns solid-like at around 3500 K. This leads mostly to filled amorphous carbon particles, as indicated by the high similarity to amorphous carbon (Fig. 4 C, left panel). At the very end of the simulations, similarity to fullerenes reaches similar values across different quenching rates, which correlates with the fact that some of the particles may reorganize into partly hollow structures.

At this final stage, three-coordinated atoms dominate, even though they are less numerous compared to slower quenching. This is mostly because the particles do contain fewer atoms, with some low coordinated atoms in separated small clusters and chains. Compared to slower quench rates, a higher number of 4-coordinated atoms is found here, even though their total amount remains very limited. Due to the peculiarities of the Tersoff potential, we may expect that the fraction of 4-coordinated atoms is likely to be underestimated here [54]. Nonetheless, the picture is confirmed by the global indicators: the gyration radius is small compared to the other simulations due to the (partial) filling of the particles and the reduced number of atoms they contain. Asphericity is relatively low for these mostly spherical, but internally disordered particles. In agreement with the two observations above, local environments in the final structure are rather similar to amorphous carbon, as reported in Fig. 4 C, left panel.

At intermediate quenching rates (center column in Fig. 4), the particles transition into more hollow structures at around 4500 K where their condensation pathway clearly diverges from the one of the system with the highest quench rate. The number of three-coordinated atoms increases significantly as many of the dangling bonds are healed, and the structure becomes locally two-dimensional. This reorganization into more hollow particles is accompanied by a sudden increase in gyration radius. The obtained fullerene-like particles are rigid, mostly asymmetric, and contain in many cases two shells. The kernel similarity index indeed is able to discern such features, indicating the highest resemblance to fullerenes at the latest stages of the simulations when the temperature is decreased below 3500 K. In this final stage of the simulation, the similarity to amorphous carbon instead clearly decreases.

In the case of the lowest quench rates (right column in Fig. 4), the transition to hollow, sometimes double-walled, fullerenes occurs at slightly higher temperatures and is more marked. The gyration radius, for instance, increases faster and further, which is correlated to a higher fraction of single-walled fullerenes. In comparison to the intermediate quench rate, some smaller differences occur in the very end of the simulations, where the similarity to carbon nanotubes increases faster and becomes the majority fraction in the final products, albeit by a small margin. This is due to another reorganization of the structures, which takes place when they are already in a solid-like state. The transition from dense amorphous to hollow structures is gradual and takes place slowly, which is why it is not observed at high quench rates, where there is not enough time to overcome the energy barriers required for the structural reorganization. This second restructuring reduces curvature in one direction and allows healing of some defects.

4. Conclusion

In this work, we use molecular dynamics to simulate the physical synthesis of carbon nanostructures. Thereby, we address the effect of initial gas density and quenching rate on the final structure. To characterize the latter, we adopt an analysis toolbox which comprises traditional local and global order parameters based on the coordination number and gyration tensor, as well as a data-driven approach that exploits local density descriptors and kernel similarity measurements. The

complementary analysis methods quantitatively characterize the carbon nanostructure evolution and allow charting the mechanistic pathway in the nanostructure formation.

We observe that extremely fast annealing rates (700 K/ns) lead to the synthesis of amorphous nanostructures. Slower rates favor the formation of fullerene-like (and nanotube-like, to a slightly lesser extent) morphologies. By adopting a structural characterization which leverages diverse order parameters, we further establish a dynamical picture of the condensation process. We find that the nucleation of small carbon nanoclusters takes place between 10000 K and 5000 K. Later, a phase change corresponding to the formation of a larger nanostructure takes place between 5000 K and 4000 K, which is more amorphous or fullerene-like depending on the annealing rate. The melting temperature of nanocarbons with the Tersoff potential is in the range of 4000 to 5,000 K. Ref. [55] for instance, indicates the melting temperature for nanotubes at around 4,800 K. In experiments, the melting point is lower, in the range of 2850 to 3300 K [56]. Due to the rather rapid cooling in our simulations and the peculiarities of the Tersoff potential, it is not very surprising that we obtain transition temperatures at the upper end of the spectrum reported in the literature. Finally, minor structural rearrangements are observed between 4000 K and 3000 K.

Besides providing some insights on the complexity of the carbon experimental synthesis via gas-phase nucleation, we believe our work will pave the way to explore other initial conditions (e.g., other gas densities), as well as other materials (e.g., silicon, boron, and transition metal dichalcogenides), which allow for the formation of non-carbon fullerenes and nanotube-like (hetero-)structures.

Declaration of Competing Interest

The authors declare that they have no known competing financial interests or personal relationships that could have appeared to influence the work reported in this paper.

Data availability

Data will be made available on request.

Acknowledgement

K.R. received funding from the European Research Council (ERC) under the European Union's Horizon 2020 research and innovation programme (Marie Curie Individual Fellowship Grant agreement No. 890414). G.D.F. acknowledges support from the Federation CaSci-ModOT (CCSC Orleans-Tours, France) that gave us access to the Region Centre computing grid. C.Z acknowledges funding from the European Union's Horizon 2020 research and innovation program (Grant No. 824143, MaX 'MAterials design at the eXascale' Centre of Excellence). J.L. acknowledges financial support of the Fonds de la Recherche Scientifique - FNRS. Computational resources have been provided by the Consortium des Equipements de Calcul Intensif (CECI) and by the Fédération Lyonnaise de Modélisation et Sciences Numeriques (FLMSN). The authors thank Andrea Anelli for insightful discussions.

Supplementary material

Supplementary material associated with this article can be found, in the online version, at [10.1016/j.cartre.2023.100268](https://doi.org/10.1016/j.cartre.2023.100268).

References

- [1] B.S. Harrison, A. Atala, *Biomaterials* 28 (2007) 344–353.
- [2] W. Hoenlein, F. Kreupl, G.S. Duesberg, A.P. Graham, M. Liebau, R.V. Seidel, E. Unger, *IEEE Trans. Compon. Packag. Technol.* 27 (2004) 629–634.
- [3] M.M. Shulaker, G. Hills, N. Patil, H. Wei, H.-Y. Chen, H.-S.P. Wong, S. Mitra, *Nature* 501 (2013) 526–530.
- [4] N. Anzar, R. Hasan, M. Tyagi, N. Yadav, J. Narang, *Sensors Int.* 1 (2020) 100003.
- [5] G. Gruner, *Anal. Bioanal. Chem.* 384 (2006) 322–335.

- [6] A.M.K. Esawi, M.M. Farag, *Mater. Des.* 28 (2007) 2394–2401.
- [7] N.F. Goldshleger, *Fullerene Sci. Technol.* 9 (2001) 255–280.
- [8] S. Bosi, T.D. Ros, G. Spalluto, M. Prato, *Eur. J. Med. Chem.* 38 (2003) 913–923.
- [9] L. Matija, R. Tsenkova, J. Munčan, M. Miyazaki, K. Banba, M. Tomić, B. Jeftić, *Fullerene based nanomaterials for biomedical applications: Engineering, functionalization and characterization*, Trans Tech Publications Ltd, 2013. Vol. 633
- [10] D. Amans, M. Diouf, J. Lam, G. Ledoux, C. Dujardin, *J. Colloid Interface Sci.* 489 (2017) 114–125.
- [11] D. Amans, A.-C. Chenus, G. Ledoux, C. Dujardin, C. Reynaud, O. Sublemontier, K. Masenelli-Varlot, O. Guillois, *Diamond Relat. Mater.* 18 (2009) 177. ISSN 0925-9635
- [12] H. Zhang, K. Chen, Y. He, Y. Zhu, Y. Chen, C. Wu, J. Wang, J.H. Liao, S.H. Liu, *J. Phys. Chem. Solids* 62 (2001) 2007–2010.
- [13] C.D. Scott, S. Arepalli, P. Nikolaev, R.E. Smalley, *Appl. Phys. A* 72 (2001) 573–580.
- [14] S. Yang, H. Zeng, H. Zhao, H. Zhang, W. Cai, *J. Mater. Chem.* 21 (2011) 4432–4436.
- [15] J. Schwan, S. Ulrich, H. Roth, H. Ehrhardt, S.R.P. Silva, J. Robertson, R. Samlenski, R. Brenn, *J. Appl. Phys.* 79 (1996) 1416–1422.
- [16] M.D. Tucker, R. Ganesan, D.G. McCulloch, J.G. Partridge, M. Stueber, S. Ulrich, M.M.M. Bilek, D.R. McKenzie, N.A. Marks, *J. Appl. Phys.* 119 (2016) 155303.
- [17] S. Li, Y. Ren, P. Biswas, S.D. Tse, *Prog. Energy Combust. Sci.* 55 (2016) 1–59.
- [18] J. Lam, D. Amans, F. Chaput, M. Diouf, G. Ledoux, N. Mary, K. Masenelli-Varlot, V. Motto-Ros, C. Dujardin, *Phys. Chem. Chem. Phys.* 16 (2013) 963–973.
- [19] J. Lam, V. Motto-Ros, D. Misiak, C. Dujardin, G. Ledoux, D. Amans, *Spectrochim. Acta, Part B* 101 (2014) 86–92.
- [20] P. Lorazo, L.J. Lewis, M. Meunier, *Phys. Rev. Lett.* 91 (2003) 225502.
- [21] L.V. Zhigilei, *Appl. Phys. A* 76 (2003) 339–350.
- [22] L.V. Zhigilei, Z. Lin, D.S. Ivanov, *J. Phys. Chem. C* 113 (2009) 11892–11906.
- [23] G.D. Förster, L.J. Lewis, *Phys. Rev. B* 97 (2018) 224301.
- [24] P. Lorazo, L.J. Lewis, M. Meunier, *Phys. Rev. B* 73 (2006) 134108. ISSN 2469-9969
- [25] J. Zhao, V. Singh, P. Grammatikopoulos, C. Cassidy, K. Aranishi, M. Sowwan, K. Nordlund, F. Djurabekova, *Phys. Rev. B* 91 (2015) 035419.
- [26] P. Krasnochtchekov, R.S. Averback, *J. Chem. Phys.* 122 (2005) 044319.
- [27] P. Krasnochtchekov, K. Albe, Y. Ashkenazy, R.S. Averback, *J. Chem. Phys.* 123 (2005) 154314.
- [28] E. Kesälä, A. Kuronen, K. Nordlund, *Phys. Rev. B* 75 (2007) 174121.
- [29] I. Parsina, F. Baletto, *J. Phys. Chem. C* 114 (2010) 1504–1511.
- [30] V. Singh, C. Cassidy, P. Grammatikopoulos, F. Djurabekova, K. Nordlund, M. Sowwan, *J. Phys. Chem. C* 118 (2014) 13869–13875.
- [31] D. Nelli, R. Ferrando, *Nanoscale* 11 (2019) 13040–13050.
- [32] G.D. Förster, M. Benoit, J. Lam, *Phys. Chem. Chem. Phys.* 21 (2019) 22774–22781.
- [33] K. Rossi, L.B. Pártay, G. Csányi, F. Baletto, *Sci. Rep.* 8 (2018) 1–9.
- [34] J. Amodeo, F. Pietrucci, J. Lam, *J. Phys. Chem. Lett.* 11 (2020) 8060–8066.
- [35] S. Plimpton, *J. Comput. Phys.* 117 (1995) 1–19.
- [36] J.T. Tersoff, J. Tersoff, *Phys. Rev. B Condens. Matter* 39 (1989) 5566. ISSN 5566-5568
- [37] J.T. Tersoff, J. Tersoff, *Phys. Rev. B Condens. Matter* 41 (1990) 3248. ISSN 5566-5568
- [38] C.J. de Tomas, J. Dethomas, *Carbon N.Y.* 109 (2016) 681–693. ISSN 681-693
- [39] M.Y. Magnin, J. Magnin, *J. Phys. Condens. Matter* 26 (2014) 185401. ISSN 185401
- [40] A.C.T. van Duin, S. Dasgupta, F. Lorant, W.A. Goddard, *J. Phys. Chem. A* 105 (2001) 9396. ISSN 1089-5639
- [41] J.H. Los, A. Fasolino, *Phys. Rev. B Condens. Matter* 68 (2003) 024107. ISSN 0163-1829
- [42] V.L. Deringer, G. Csanyi, *Phys. Rev. B Condens. Matter* 95 (2017) 094203. ISSN 0163-1829
- [43] L.M. Mejia-Mendoza, M. Valdez-Gonzalez, J. Muniz, U. Santiago, A.K. Cuentas-Gallegos, M. Robles, *Carbon N. Y.* 120 (2017) 233. ISSN 0008-6223
- [44] D. Franzblau, *Phys. Rev. B* 44 (1991) 4925.
- [45] R. Meissner, <https://github.com/jaaproe/polypy>.
- [46] S. Sarangi, B. Bhargava, S. Balasubramanian, *Phys. Chem. Chem. Phys.* 11 (2009) 8745–8751.
- [47] R. Drautz, *Phys. Rev. B* 99 (2019) 014104.
- [48] G. Dussan, M. Bachmayr, G. Csanyi, R. Drautz, S. Etter, C. van der Oord, C. Ortner, 2019, *ArXiv preprint arXiv:1911.03550*.
- [49] C. Ortner, ACE.jl (2019). <https://github.com/ACEsuit/ACE.jl/tree/dev-v0.8.x>
- [50] C. Zeni, K. Rossi, A. Glielmo, S. De Gironcoli, *J. Chem. Phys.* 154 (2021) 224112.
- [51] Y. Lysogorskiy, C. van der Oord, A. Bochkarev, S. Menon, M. Rinaldi, T. Hammer-schmidt, M. Mrovec, A. Thompson, G. Csányi, C. Ortner, R. Drautz, *npj Comput. Mater.* 1 (2021) 1–12.
- [52] C. Zeni, K. Rossi, T. Pavloudis, J. Kioseoglou, S. de Gironcoli, R. Palmer, F. Baletto, *Nat. Commun.* 12 (2021).
- [53] D.P. Kovacs, C. van der Oord, J. Kucera, A. Allen, D. Cole, C. Ortner, G. Csanyi, *chemarxiv* (2021).
- [54] X. Li, A. Wang, K.R. Lee, *Comput. Mater. Sci.* 151 (2018) 246. ISSN 0927-0256
- [55] K. Zhang, G.M. Stocks, J. Zhong, *Nanotechnology* 18 (2007) 285703. ISSN 0957-4484
- [56] E. Ganz, A.B. Ganz, L.-M. Yang, M. Dornfeld, *Phys. Chem. Chem. Phys.* 19 (2017) 3756. ISSN 1463-9076, 1463-9084